Optics & Laser Technology 183 (2025) 112315

Contents lists available at ScienceDirect

Optics and Laser Technology

journal homepage: www.elsevier.com/locate/optlastec

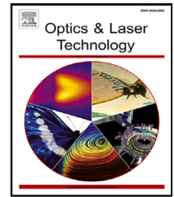

Full length article

Efficient nonlinear resist modeling by combining and cascading quadratic Wiener systems

Chunxiao Mu [a], Lei Cheng [a], Song Zhang [b], Hao Jiang [a,d,*], David H. Wei [b,**], Yanlong Sun [c], Jinlong Zhu [a], Shiyuan Liu [a,d,*]

[a] School of Mechanical Science and Engineering, Huazhong University of Science and Technology, Wuhan, 430074, Hubei, China
[b] Yuwei Optica Co., Ltd, Wuhan, 430070, Hubei, China
[c] Institute of Artificial Intelligence, Hefei Comprehensive National Science Center, Hefei, 230088, Anhui, China
[d] Optics Valley Laboratory, Wuhan, 430074, Hubei, China

ARTICLE INFO

Keywords:
OPC
Computational lithography
Nonlinear resist system modeling
Performance optimization
Model calibration method

ABSTRACT

Optical proximity correction (OPC) is currently a crucial technique for improving photolithographic image quality, with its correctness and efficiency relying heavily on resist modeling. The resist exposure and development processes involve various complex nonlinear physicochemical reactions, which impose a great challenge to model in a fast and accurate manner that meets the requirements of OPC. In this paper, we propose a set of solutions for nonlinear resist modeling, including a multi-stage cascaded quadratic Wiener model network, a simulation acceleration method using eigendecomposition, and an efficient method of model calibration utilizing the projected Landweber method. Various experiments are conducted for validation, which demonstrate that a single-stage Wiener model may already meet the usual requirements for production worthiness, while a multi-stage model achieves even better performance in terms of model accuracy, generality, and speed. The proposed resist modeling method holds great potential in advancing photolithography modeling and OPC for modern semiconductor manufacturing.

1. Introduction

Optical proximity correction (OPC) stands as a crucial technique for mask optimization in photolithography, employing an iterative approach where its efficacy is fundamentally linked to the accuracy of the lithography model. Currently, advanced full-chip simulation technologies primarily adopt separate optical, mask, and resist models to achieve computational efficiency, accuracy, and applicability [1]. Among them, the resist model describes the intricate interplay between light and materials coupled with the nonlinear physicochemical processes, which plays a pivotal role in photolithography process analysis and directly determines the efficiency and performance of mask optimization. As shown in Fig. 1, the key resist-related steps in lithography generally include soft bake, exposure, post-exposure bake (PEB), and development. In these processes, there are diffusion, neutralization, decomposition, and polymerization involved and should be efficiently and accurately characterized [2]. Therefore, the resist model can be regarded as a complex nonlinear system modeling that transforms the input aerial image into the resist profile, which often encounters several challenges due to their inherent properties [3–5]. For instance,

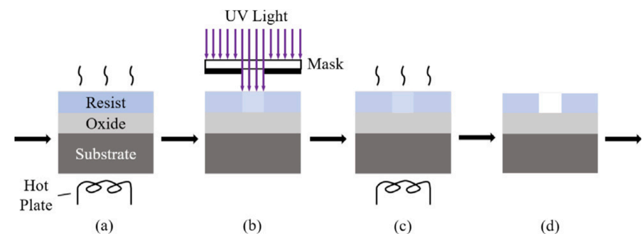

Fig. 1. Illustration of resist process: (a) post apply bake, also called soft bake, (b) alignment and exposure, (c) PEB, (d) development.

the separation of the coupling of complex physicochemical reactions with simple linear equations, the time-consuming and labor-intensive model calibration and verification with extensive data, and the high-dimensional models induced extra computational costs, may limit their practical applications.

* Corresponding authors at: School of Mechanical Science and Engineering, Huazhong University of Science and Technology, Wuhan, 430074, Hubei, China.
** Corresponding author at: Yuwei Optica Co., Ltd, Wuhan, 430070, Hubei, China.
E-mail addresses: hjiang@hust.edu.cn (H. Jiang), david.hq.wei@gmail.com (D.H. Wei), shyliu@hust.edu.cn (S. Liu).

https://doi.org/10.1016/j.optlastec.2024.112315
Received 23 June 2024; Received in revised form 14 October 2024; Accepted 10 December 2024
0030-3992/© 2024 Elsevier Ltd. All rights are reserved, including those for text and data mining, AI training, and similar technologies.

The earliest widely used photoresist calibration methods are the threshold models, including the constant threshold resist (CTR) model and the variable threshold resist (VTR) model. These models are usually computationally efficient and are typically specific to a single lithography process under particular conditions. Since their calibration results may not be readily transferable to different substrates or process variations, their applications are limited [6,7]. Additionally, due to the simplicity, they fail to accurately simulate the post-development morphology of resists [8,9].

In contrast, the rigorous physical resist models employing differential equation solving techniques, finite difference methods, or other approaches can precisely describe the three-dimensional morphology for resists after a series of complex physicochemical changes during the lithography process. However, the complexity of these models poses significant challenges [10–12]. Additionally, extensive critical dimension data and numerous complex physicochemical parameters that are difficult to directly measure are required in their model calibration [13]. Most importantly, these models are typically only suitable for small area predictions due to their slow computation speed.

The compact models such as CM1 express lithography results as a linear combination of convolutions between different aerial images and Laguerre–Gaussian kernels. By selecting aerial images of different powers, derivatives, and biases, the model effectively describes various nonlinear effects during the post-exposure and development processes [14–16]. The CM1 model achieves a good balance between accuracy and computational efficiency, making it one of the most widely used models in the field of full-chip simulations and OPC.

Benefiting from the capability of capturing the difficult-to-describe physicochemical effects and unknown effects not included in the rigorous physical models [17–19], AI models may achieve higher OPC accuracy than traditional models and therefore have attracted comprehensive attention during recent years. AI models employ machine learning or deep learning algorithms to automatically learn the behavior of resist from a vast dataset of CD-SEM images. However, AI models lack physical interpretability and require extensive highly empirical hyperparameter tuning. Additionally, the training and calibration accuracy of an AI model strongly depends on the input aerial image precision, i.e. AI model is highly sensitive to the input data, where minor perturbations may lead to significantly different results [20,21].

In this paper, we propose a comprehensive nonlinear resist modeling solution based on a multi-stage cascaded Wiener model network. In Section 2, we present the construction of this resist model, and corresponding acceleration techniques based on linear superposition and eigenvalue decomposition, along with a calibration method utilizing the projected Landweber method. In Section 3, we show the experimental results for validation and the results show that both the single-stage and multi-stage Wiener models can meet industry standards, while the multistage Wiener model outperforms the single-stage model in all respects. And then conclusions are drawn in Section 4.

2. Theory and methods

2.1. General Wiener system modeling for nonlinear resist processes

The Stone–Weierstrass theorem states that any continuous functional on a compact domain can be uniformly approximated by a sequence of functionals of integer order. Therefore, the system response of the resist model can be expressed with Volterra series [22,23] as:

$$R_n[I(x)]=\sum_{n=0}^{\infty}\left[\int\cdots\int h\left(x_1,x_2,\ldots,x_n\right)\prod_{i=1}^{n} I\left(x-x_i\right)\,dx_1\,dx_2\ldots dx_n\right], \tag{1}$$

where, the nth order nonlinear system response function and $h\left(x_1,x_2,\ldots,x_n\right)$ represents the resist's response to the nth input optical intensity distribution. While this expression provides an analytical and rigorous mathematical representation, it is worth noting that in the process of system response characterization and modeling, particularly for the nonlinear parts represented by multi-dimensional high-order Volterra kernels, calibration requires a significant amount of measurement data. Given the high storage costs and the complexity of computations involved, this becomes impractical.

To address these issues, we utilize the normalized orthogonal functions and finite-dimensional approximation theories to achieve a reduced-dimensional representation of the high-order Volterra kernel functions [24]. Specifically, within a compact domain, it is possible to represent any function within that domain using a set of orthogonal normalized functions with a given error tolerance [25–27]. Therefore, for the Stone–Wiener theorem based nth order nonlinear resist model, it can be expressed by the following closed-form,

$$R[I]\approx\sum_{n=1}^{N}\left[\sum_{\{k_i\}=1}^{K} w_{k_1k_2\ldots k_n}\left(H_{k_1}\otimes I\right)\left(H_{k_2}\otimes I\right)\cdots\left(H_{k_n}\otimes I\right)\right], \tag{2}$$

where, the orthonormal functions H_{k_n} are Wiener kernels, and $w_{k_1k_2\ldots k_n}$ are Wiener coefficients.

It is important to emphasize that, in order to reduce the simulation errors introduced by geometric transformations, we need to select a set of orthogonal basis functions that possess circular symmetry, rotational, and translational invariance. In this paper, we choose the Laguerre-Gaussian basis functions as the Wiener kernel functions [28–30]:

$$H_{s,m,n}(x,y)=\frac{1}{\pi s^2}L_n^m\left(2\frac{r^2}{s^2}\right)\exp\left(-\frac{r^2}{s^2}\right)\exp\left(im\phi\right), \quad r^2=x^2+y^2,\ \phi=\tan^{-1}(y/x) \tag{3}$$

where s represents the continuous diffusion length, and $L_n^m(x)$ represents the associated Laguerre polynomial, which can be expressed with Rodrigues representation:

$$L_n^m(x)=\frac{e^x x^{-m}}{n!}\frac{d^n}{dx^n}\left(e^{-x}x^{n+m}\right). \tag{4}$$

We utilize the following recursive formula for numerical computation:

$$L_{n+1}^m(x)=\frac{1}{n+1}\left[(2n+m+1-x)\,L_n^m(x)-(n+m)\,L_{n-1}^m(x)\right], \tag{5}$$

where $L_0^m(x)=1$ and $L_0^m(x)=-x+m+1$.

Fig. 2 illustrates the intensity distribution of the Laguerre-Gaussian kernel function with varying n and m. When both n and m are zeros, the figure represents the simplest form of the Gaussian kernel function, characterized by its highest symmetry and peak intensity. As m increases while n remains constant, the initially circularly symmetric kernel function splits into one or even two sets of patterns with m-fold rotational symmetry, composed of positive and negative intensities. When n increases and m remains constant, the kernel function's influence expands, spreading outward. By selecting appropriate model parameters, we can build efficient and accurate models of different types of resists.

2.2. Formulation of multi-stage cascaded quadratic Wiener model network

Theoretically, the Wiener model described in Eq. (2) should be able to simulate the actual resist responses. However, all its terms and operations are coupled at a single stage, leading to significantly increased modeling complexity and calibration difficulty. To reduce the system complexity and enhance flexibility, fault tolerance, and scalability, we design a multi-stage network that chains multiple Wiener models together, limiting the nonlinearity of the Wiener model at each stage to at most quadratic terms. Through a cascading series of quadratic terms, this model can accurately reconstruct the overall higher-order resist responses with the simplicity of sub-models. The basic workflow is illustrated in Fig. 3. The aerial images are sequentially propagated through a cascaded Wiener model network, stage by stage, transforming into the final resist image.

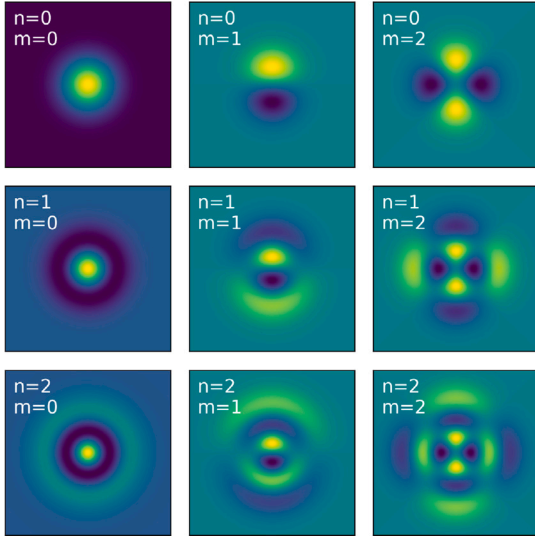

Fig. 2. Illustration of the intensity distribution of the Laguerre-Gaussian kernel function in relation to changes in its parameter n and m.

As depicted in Fig. 3(a), in the first stage, the input is the aerial image intensity distribution projected onto the resist surface. By convolving it with several custom Wiener kernels, which are based on the Laguerre–Gaussian functions described in Eq. (3), we obtain the Wiener bases, which also serve as the linear terms. Then, we construct the quadratic terms from element-wise multiplication of the Wiener bases. All linear and quadratic terms are collectively referred to as Wiener products (WPs). The output of this stage is the sum of the Wiener products weighted with calibrated Wiener coefficients:

$$R(x,y) = \sum_i w_i \mathrm{WP}_i(x,y). \tag{6}$$

As shown in Fig. 3(b), we adjust the number of Wiener kernels and combinations of linear and quadratic terms, then carry out the same operations before passing the output to the next stage. This process continues, until we obtain the resist contours by truncating the image with a calibrated resist threshold. Overall, we minimize the use of resist terms, which reduces computational complexity and runtime, while maintaining flexibility in model calibration. Compared to calibrating all terms at once, this staged approach helps avoid overfitting by progressively adjusting the model's complexity.

2.3. Efficient Wiener model construction method

For Wiener systems described by Eq. (6), we can reorganize its terms to reduce the computational complexity.

We can first combine all linear terms into a single convolution operation using a single accumulated Wiener kernel:

$$\mathbf{R}_L = \sum_i w_i \left(\mathbf{H}_i \otimes \mathbf{I}\right) = \left(\sum_i w_i \mathbf{H}_i\right) \otimes \mathbf{I} = \mathbf{G} \otimes \mathbf{I}. \tag{7}$$

By using just one kernel $\mathbf{G} = \sum_i w_i \mathbf{H}_i$, we can reduce the computation time for $n-1$ convolution operations during the OPC forward modeling process.

For quadratic terms, we first perform an eigendecomposition on the Wiener coefficients to decrease the complexity of computation from $O(n^2)$ to $O(n)$. Assuming symmetrical coefficients $w_{ij} = w_{ji}$, the quadratic output can be expressed as

$$\mathbf{R}_Q = \sum_{ij} w_{ij} \left(\mathbf{H}_i \otimes \mathbf{I}\right)\left(\mathbf{H}_j \otimes \mathbf{I}\right). \tag{8}$$

If we precompute all the convolutional outputs, the computational complexity is $O(n^2)$. We can simplify Eq. (8) by utilizing the quadratic structure. We first convert the coefficient matrix w_{ij} into a diagonal matrix, denoted by $\mathbf{W} = \mathbf{U}^{\dagger}\mathbf{D}\mathbf{U}$, where $\mathbf{W}$ is the matrix with elements w_{ij}, $\mathbf{U}$ is a unitary matrix, and $\mathbf{D}$ is a diagonal matrix with eigenvalues $\lambda_1, \lambda_2, \ldots, \lambda_n$. We define block matrices as

$$\mathbf{H} \overset{\text{def}}{=} \begin{bmatrix} H_1 \\ H_2 \\ \vdots \\ H_n \end{bmatrix}, \mathbf{P} \overset{\text{def}}{=} \mathbf{H} \otimes \mathbf{I} = \begin{bmatrix} R_1 \\ R_2 \\ \vdots \\ R_n \end{bmatrix}, \mathbf{G} \overset{\text{def}}{=} \mathbf{U}\mathbf{H} = \begin{bmatrix} G_1 \\ G_2 \\ \vdots \\ G_n \end{bmatrix}.$$

Following this, Eq. (8) is transformed into:

$$\begin{aligned} \mathbf{R}_Q &= \sum_{i,j} w_{ij} \mathbf{P}_i \mathbf{P}_j \\ &= \mathbf{P}^{\mathrm{T}} \mathbf{W} \mathbf{P} \\ &= (\mathbf{I} \otimes \mathbf{H}\mathbf{U})^{\mathrm{T}} \mathbf{D} (\mathbf{U}\mathbf{H} \otimes \mathbf{I}) \\ &= (\mathbf{I} \otimes \mathbf{G})^{\mathrm{T}} \mathbf{D} (\mathbf{G} \otimes \mathbf{I}) \\ &= \sum_i \lambda_i (\mathbf{G}_i \otimes \mathbf{I})^2. \end{aligned} \tag{9}$$

The complexity is reduced to $O(n)$.

2.4. Wiener model calibration method based on the projected Landweber method

The proposed multi-stage cascaded quadratic Wiener model network offers considerable flexibility, allowing for its calibration process to be conducted stage-by-stage. If the calibration result at any stage meets the requirements, the Wiener model network can be truncated at that point. In practice, OPC models are calibrated using the CD lengths. For the Wiener model, resist model calibration can be regarded as a parameter estimation problem, where the objective is to find the parameters that make the model predicted CD lengths fit the best with the actual measured values. Given the multitude of parameters in the resist model, finding the optimal solution in a high-dimensional parameter space is challenging [31–33]. For the Wiener model calibration of each stage, we employ the projected Landweber method [34] to optimize the Wiener coefficients by gradually adjusting the coefficients to reduce CD error. This method has the advantage of being computationally efficient and memory-friendly, making it particularly suitable for handling large, high-dimensional matrices often encountered in resist model calibration. We search for the optimal perturbation $\{\delta w_n^{(k)}\}_{n=0}^{N}$ at the kth iteration by defining and minimizing the following objective function:

$$\min \|\mathbf{A}^{(k)}\delta\mathbf{w}^{(k)} + \mathbf{e}^{(k)}\|^2 = \sum_{m=1}^{M}\left(\sum_{n=0}^{N} A_{mn}^{(k)}\delta w_n^{(k)} + \Delta\mathrm{CD}_m\right)^2, \tag{10}$$

where, M means the number of measured CDs, $\Delta\mathrm{CD}_m$ is the difference between the simulated CD by the Wiener model and the actual measured CD for the mth measurement. $\mathbf{e}^{(k)} = \left[\Delta\mathrm{CD}_1, \Delta\mathrm{CD}_2, \ldots, \Delta\mathrm{CD}_M\right]^T$ is a column vector of CD simulation errors, $\delta\mathbf{w}^{(k)} = \left[\delta w_0^{(k)}, \delta w_1^{(k)}, \ldots, \delta w_N^{(k)}\right]^T$ is a column vector of adjustments to the Wiener coefficients, and $\mathbf{A}^{(k)}$ is a linear operator represented in a matrix form $\mathbf{A}^{(k)} = \left[A_{mn}^{(k)}\right]_{mn}$ with

$$A_{mm}^{(k)} = \frac{\mathrm{WP}_n\left(x_m, y_m\right)}{\mathrm{SL}^{(k)}\left(x_m, y_m\right)} + \frac{\mathrm{WP}_n\left(x_m', y_m'\right)}{\mathrm{SL}^{(k)}\left(x_m', y_m'\right)}, \\ \forall m \in [1, M], \forall n \in [0, N]. \tag{11}$$

$\mathrm{WP}_n\left(x_m, y_m\right)$ and $\mathrm{WP}_n\left(x_m', y_m'\right)$ are the Wiener products at the start and end points. The spatial slopes

$$\mathrm{SL}^{(k)}(x,y) = \sum_{n=0}^{N} w_n^{(k)} \mathrm{SL}_n(x,y), \tag{12}$$

$\mathrm{SL}^{(k)}(x_m', y_m')$ and $\Delta\mathrm{CD}_m$ are computed based on the Wiener coefficients $\{w_n^{(k)}\}_{n=0}^{N}$ at the beginning and treated as constants for the remaining

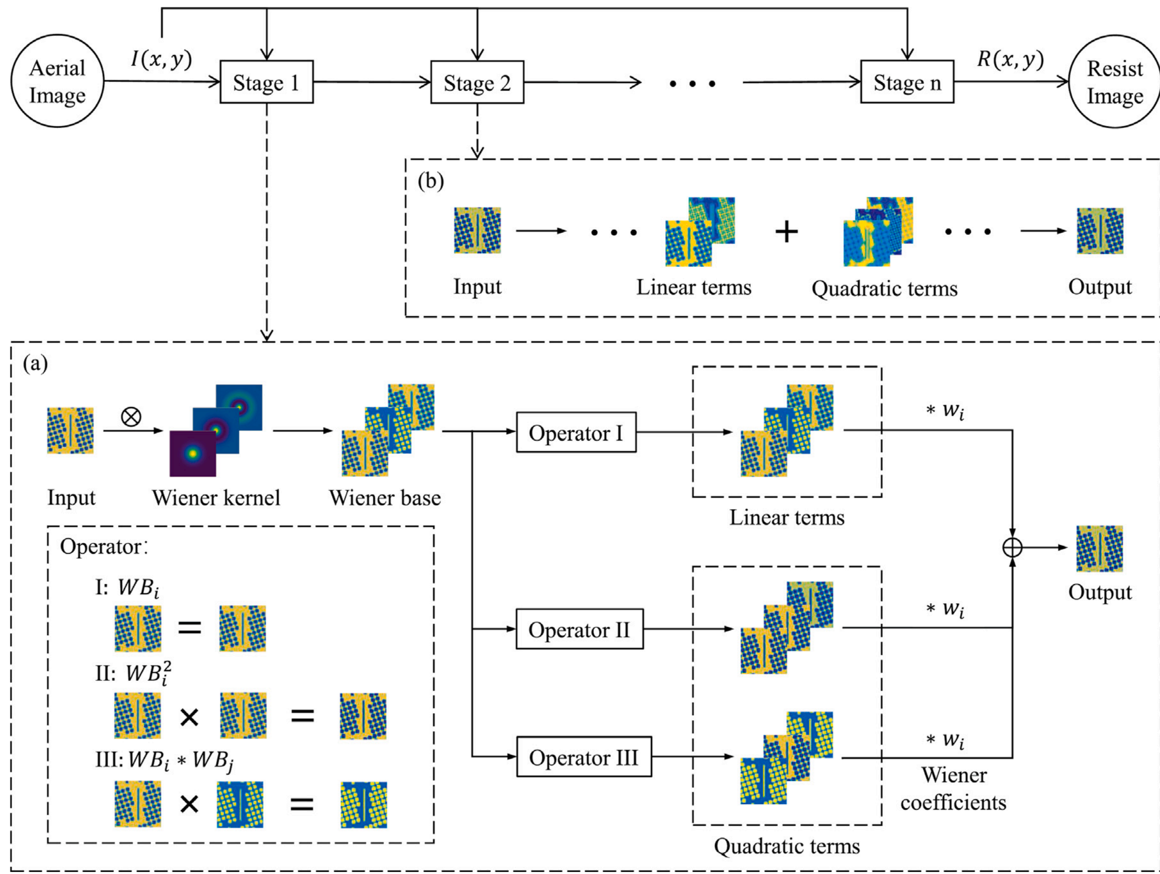

Fig. 3. Illustration of the multi-stage cascaded quadratic Wiener model network: (a) the image propagation mechanism within a single-stage network, (b) similar image propagation mechanism based on custom-defined parameters in the subsequent stage.

of the kth iteration. Note that the slope directions of the endpoints are different:

$$\mathrm{SL}_n(x_m, y_m) = \frac{\mathrm{WP}_n(x_m+\Delta x, y_m) - \mathrm{WP}_n(x_m-\Delta x, y_m)}{2\Delta x},$$
$$\mathrm{SL}_n(x'_m, y'_m) = \frac{\mathrm{WP}_n(x'_m-\Delta x, y'_m) - \mathrm{WP}_n(x'_m+\Delta x, y'_m)}{2\Delta x}. \tag{13}$$

Wiener coefficients $\{w_n\}_{n=0}^{N}$ are updated at the kth iteration according to the following formula:

$$\delta \mathbf{w}^{(k)} = \mathbf{w}^{(k+1)} - \mathbf{w}^{(k)} = -\tau\left[\mathbf{A}^{(k)}\right]^{\dagger}\mathbf{e}^{(k)}, \forall k \geq 0, \tag{14}$$

that is,

$$\mathbf{w}^{(k+1)} = \mathbf{w}^{(k)} - \tau\left[\mathbf{A}^{(k)}\right]^{\dagger}\mathbf{e}^{(k)}, \forall k \geq 0 \tag{15}$$

where $\left[\mathbf{A}^{(k)}\right]^{\dagger}$ is the conjugate matrix of $\mathbf{A}^{(k)}$, and τ is a critical tuning parameter in the projected Landweber method, impacting how the Wiener model coefficients converge during calibration to achieve optimal accuracy.

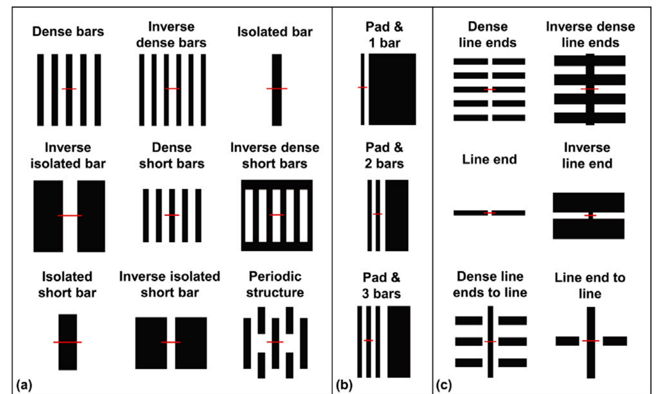

Fig. 4. The training patterns for model calibration: (a) 1D, (b) 1.5D, (c) 2D.

3. Experimental results

We have conducted a series of experiments in a DUV immersion lithography system with an illumination wavelength of 193 nm, an NA of 1.2, a 6% attenuated phase shift mask with bright field, and a PTD resist. The simulations were carried out on a real poly layer with feature sizes ranging from 40 nm to 500 nm. Our comprehensive dataset comprises more than 3000 patterns, featuring 1D, 1.5D, and 2D structures. Within these, over 100 patterns are designed for verification, while the remainder are utilized for calibration. Key characteristic structures within this collection are depicted in Fig. 4. The 1D patterns are variations of dense and isolated bars, both in standard and inverse formats, including short bars and periodic structures. There are also some patterns, such as pads with one to three bars, designed to examine the interaction between isolated and dense features. While these are essentially 1D patterns, we classify them as 1.5D with higher error tolerance based on the actual process requirements. The 2D category captures the complex interactions with patterns such as dense and inverse dense line ends, and line ends to line, vital for assessing the fidelity of the resist model. Notably, these patterns are marked with red lines to denote measurement locations for model calibration.

We made a comprehensive comparison between the single-stage and the multi-stage Wiener models, with a specific focus on assessing their simulation outcomes in terms of accuracy, applicability, and computational efficiency. For the single-stage Wiener model, we added

Table 1
Comparative number of Wiener terms.

Model	Stage0		Stage1		Total
	Linear terms	Quadratic terms	Linear terms	Quadratic terms	
Single-stage	1	12	0	0	13
Multi-stage	1	4	1	4	10

a limited number of terms in a single stage to calibrate the resist model, while ensuring that the accuracy of this model was sufficient to reach the industry level. For the multi-stage Wiener model, we added terms across multiple stages to calibrate the resist model. In this paper, the single-stage Wiener model consists of a combination of 1 linear term and 12 quadratic terms within one stage, while the multi-stage Wiener model has 1 linear term and 4 quadratic terms in each of its two stages, as shown in Table 1. Experimental results indicate that the single-stage Wiener model can achieve industry standards in model accuracy, applicability, and computational efficiency. Meanwhile, the multi-stage model performs even better, with a more efficient modeling and calibration process.

3.1. Accuracy evaluation of the single-stage and the multi-stage Wiener model based on CD and contour simulation

In terms of model accuracy, we conducted a comparative analysis between the single-stage and the multi-stage Wiener model, focusing specifically on the simulation errors, which were the differences between the measured and simulated CDs. This evaluation encompassed three different structural patterns: 1D, 1.5D, and 2D. For each, we calculated parameters such as the overall Root Mean Square (RMS) and the range of errors, providing a comprehensive and quantifiable measure of performance, effectively reflecting the discrepancies between the predicted values of the two models and the actual values.

Upon a detailed comparison of the performance metrics for model calibration and verification from Table 2, it is evident that the multi-stage Wiener model exhibits superior performance when compared to the single-stage Wiener model across multiple dimensions.

Specifically, for 1D, 2D, and all patterns, the multi-stage Wiener model achieves RMS errors of 0.8375 nm, 2.0858 nm, and 0.9371 nm compared to 0.8389 nm, 2.1878 nm, and 0.9523 nm by the single-stage Wiener model, showing a slightly better fit to the data. The trend of the improved performance with the multi-stage Wiener model is more pronounced in the 1.5D patterns, where its RMS error drops significantly from 1.1831 nm to 0.8821 nm, indicating a substantially better predictive accuracy. Although the multi-stage Wiener model and the single-stage Wiener model perform differently in error range within the three intervals, in the overall range, the multi-stage model presents a narrower error range of 16.9900 nm, compared to 17.5470 nm achieved by the single-stage model, suggesting the better consistency in the predictive capability of models. The mean error is a critical metric for determining the systematic bias in the models. Ideally, this value should be as close to zero as possible. The multi-stage Wiener model outperforms in the 1.5D calibration, where its mean error drops from −1.1774 nm to −0.7366 nm. For the rest parts, the differences of the mean simulation errors between the 2 models are not obvious.

The most telling case is the verification part, where models were tested against unused data. Here, the multi-stage Wiener model exhibits a notably lower RMS value of 0.7774 nm compared to the single-stage Wiener model's RMS of 1.0505 nm, indicating a more accurate prediction capability. Furthermore, the multi-stage model has a significantly narrower error range of 4.0480 nm, compared to the single-stage model's error range of 6.9559 nm, indicating that the multi-stage model's predictions are less variable and more reliable. The mean error for the multi-stage model is 0.0789 nm, showing a slight positive bias, yet it is markedly better than the single-stage model's mean error of 0.3867 nm, which indicates a stronger tendency towards overestimation in the single-stage model's predictions during verification.

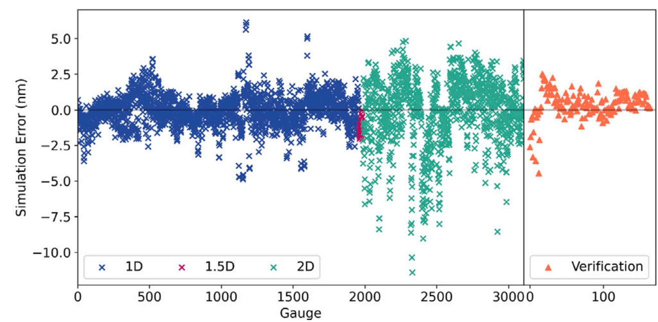

Fig. 5. Distribution of simulation errors for the single-stage Wiener model.

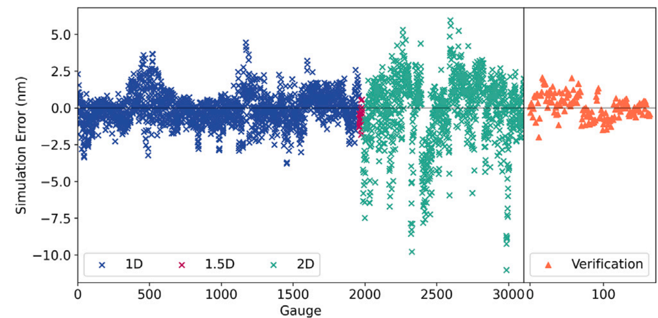

Fig. 6. Distribution of simulation errors for the multi-stage Wiener model.

To visualize the simulation error trends across different patterns, scatter plots of the simulation error distributions achieved by the single-stage and multi-stage Wiener model are provided in Figs. 5 and 6, respectively. The blue cross markers represent the CD error between simulation and measurement for 1D patterns, the red cross markers for 1.5D patterns, the green cross markers for 2D patterns, and the orange triangle markers for the verification gauge set. As shown in Fig. 5, when the single-stage Wiener model is applied, the simulation errors for 1D calibration patterns are densely clustered around the zero line, indicating a relatively small variance in errors. It is noteworthy that the errors corresponding to some patterns are much larger than those of most other patterns, even reaching about ±5 nm. These patterns are considered sub-rule patterns, included specifically to enhance the model prediction ability for smaller feature sizes. Given their purpose, larger errors in such cases are expected and acceptable. For the 1.5D patterns, while fewer in number, they also cluster near the zero line. Due to the structure being more prone to deformation, the simulation errors of 2D patterns show larger dispersion, suggesting that the model's predictions vary more in this interval. Taking the production line's reference standards for model calibration results, which are ±2.5 nm for 1D patterns, ±4 nm for 1.5D patterns, and ±6 nm for 2D patterns, into account, the simulation error for 3174 out of 3271 CDs falls within the reference range. This accounts for 97.03% of the total calibrated patterns, satisfying the requirement of the production line that the calibration results must be within the reference range for over 95% of the cases. In the verification part, the distribution of the errors is within the acceptable range, and the bulk of the errors are clustered around the zero line, which suggests that while the model may have variability in its predictions, it does not consistently overestimate or underestimate. Also, the spread of errors does not appear to be biased towards positive or negative values, implying that the single-stage model verification errors are not systematically skewed in one direction.

A comparison of Figs. 5 and 6 reveals that the multi-stage Wiener model consistently produced a more concentrated clustering of error

Table 2
Comparative performance metrics for model calibration and verification.

Type		Model	RMS (nm)	Error range (nm)	Mean error (nm)	Reference range (nm)	Within range
Calibration	1D	Single-stage	0.8389	11.0100	−0.0856	±2.5	96.89%
		Multi-stage	0.8375	8.2393	−0.0848	±2.5	97.29%
	1.5D	Single-stage	1.1831	2.0119	−1.1774	±4	100%
		Multi-stage	0.8821	2.3909	−0.7366	±4	100%
	2D	Single-stage	2.1878	16.2454	−0.1639	±6	96.97%
		Multi-stage	2.0858	16.9900	−0.1989	±6	97.06%
	ALL	Single-stage	0.9523	17.5470	−0.1230	–	97.03%
		Multi-stage	0.9371	16.9900	−0.1314	–	97.31%
Verification		Single-stage	1.0505	6.9559	0.3867	–	–
		Multi-stage	0.7774	4.0480	0.0789	–	–

points near the zero line across all calibration pattern types, signaling more accurate predictions. Compared with the single-stage model, the multi-stage model further increases the number of simulated CDs within the reference range, achieving 97.31%. Additionally, the multi-stage model tends to have fewer outliers during the 1D pattern verification. Overall, the multi-stage model's errors are more symmetrically distributed around the zero line, implying a balanced, unbiased prediction capability, especially in the context of data not previously encountered during training.

To evaluate the accuracy of simulated contours beyond the measurement points, we conducted simulations for the 18 different patterns mentioned in Fig. 4 and overlay the simulation-derived contours of two models with Scanning Electron Microscope (SEM) images in Fig. 7. The green and red contours in Fig. 7 respectively represent the simulation results of the single-stage and multi-stage Wiener Model, and the CD measurement points used for model calibration are located at the center of each image. From a quick visual evaluation, it seems that both models produce contours that generally align with the SEM images, particularly in areas of the image where the types of measurement points differ. Specifically, in the line end areas of 1D patterns and the long edge CD areas of 2D patterns, the contours simulated by both models align tightly with the actual structures.

3.2. Applicability evaluation of the single-stage and the multi-stage Wiener model based on process window and MEEF analysis

Process window in photolithographic manufacturing refers to the range of parameters, such as defocus and exposure dose, within which accurate micro-patterns can be produced. To assess the generality and applicability of the Wiener model, we conducted a process window analysis for 202 gauges. We selected 12 patterns, including six dense bars, two inverse dense bars, two line ends, and two dense line ends. Specifically, these patterns are: (a) 64 nm lines with 260 nm pitch, (b) 64 nm lines with 1500 nm pitch, (c) 58 nm lines with 116 nm pitch, (d) 80 nm spaces with 160 nm pitch, (e) 74 nm lines with 340 nm pitch, (f) 74 nm lines with 1000 nm pitch, (g) 140 nm lines with 280 nm pitch, (h) 160 nm spaces with 320 nm pitch, (i) 80 nm line with a 60 nm space between line ends, (j) 100 nm line with a 70 nm space between line ends, (k) 60 nm line with 126 nm pitch and a 150 space nm between line ends, and (l) 70 nm line with 200 nm pitch and a 150 nm space between line ends. Based on the existing measured Focus Exposure Matrix (FEM) data, we conducted simulations for these 12 patterns under different defocus conditions and plotted the Bossung curves. The defocus range in Fig. 8 spans from −60 nm to +60 nm, with a 20 nm interval. Although the measurement data trends for the last four 2D gauges are unclear due to the measurement error, the simulated CD trends for both models exhibit parabolic-like shapes, which is reasonable. Relatively, the multi-stage Wiener model shows a trend closer to the actual measurement data than the single-stage Wiener model. In addition, we also simulated these 12 patterns under different dose conditions, with a range from 0.9 to 1.1 and an interval of 0.05. Although the measurement data under different dose conditions were not provided, both models exhibit similar and reasonable trends in Fig. 9.

Table 3
Comparative modeling time.

Simulation area (μm^2)	Model	Before accelerating (s)	After accelerating (s)
5.12*5.12	Single-stage	0.06	0.01
	Multi-stage	0.04	0.01
10.24*10.24	Single-stage	0.26	0.03
	Multi-stage	0.16	0.02
20.48*20.48	Single-stage	1.84	0.12
	Multi-stage	1.32	0.09
40.96*40.96	Single-stage	10.97	0.71
	Multi-stage	6.92	0.54

Mask Error Enhancement Factor (MEEF) is also an important indicator for assessing model applicability in OPC. A higher MEEF value indicates that errors on the mask have a greater impact on the wafer patterns, resulting in lower tolerance for imaging quality. Conversely, a lower MEEF value suggests that mask errors have a smaller influence on wafer imaging. We conducted MEEF comparison experiments for both the single-stage and multi-stage models. We expanded and shrank the test patterns on the mask by 1 nm, and calculated the simulated CD for all gauges. We defined MEEF as the average of the simulated CD changes from the two experiments. The MEEF error is calculated as the difference between the MEEF of the single-stage model and the MEEF of the multi-stage model. As shown in Fig. 10(a) and (b), the MEEF for each pattern type reaches its maximum at the minimum CD and decreases as the measured CD increases. The variation range of MEEF for 2D patterns is greater than that for 1D and 1.5D patterns. Both models exhibit a similar and reasonable overall trend in MEEF. From the results in Fig. 10(c), we can see the difference in MEEF between the two models. Overall, the multi-stage model demonstrates better MEEF performance than the single-stage model for 2249 out of 3271 gauges, accounting for approximately 68.8%. Specifically, the number of gauges where the multi-stage model's MEEF is smaller than that of the single-stage model is as follows: 1D: 1398 out of 1960 (71.3%), 1.5D: 22 out of 26 (84.6%), 2D: 692 out of 1121 (61.7%), and Verification: 137 out of 164 (83.5%).

3.3. Efficiency evaluation of the single-stage and the multi-stage Wiener model based on modeling time comparison

In terms of computational efficiency, based on the performance optimization methods mentioned in Section 2.3, we varied the image size and recorded the resist modeling duration of the single-stage and the multi-stage Wiener model before and after implementing the strategy, and the results are reported in Table 3.

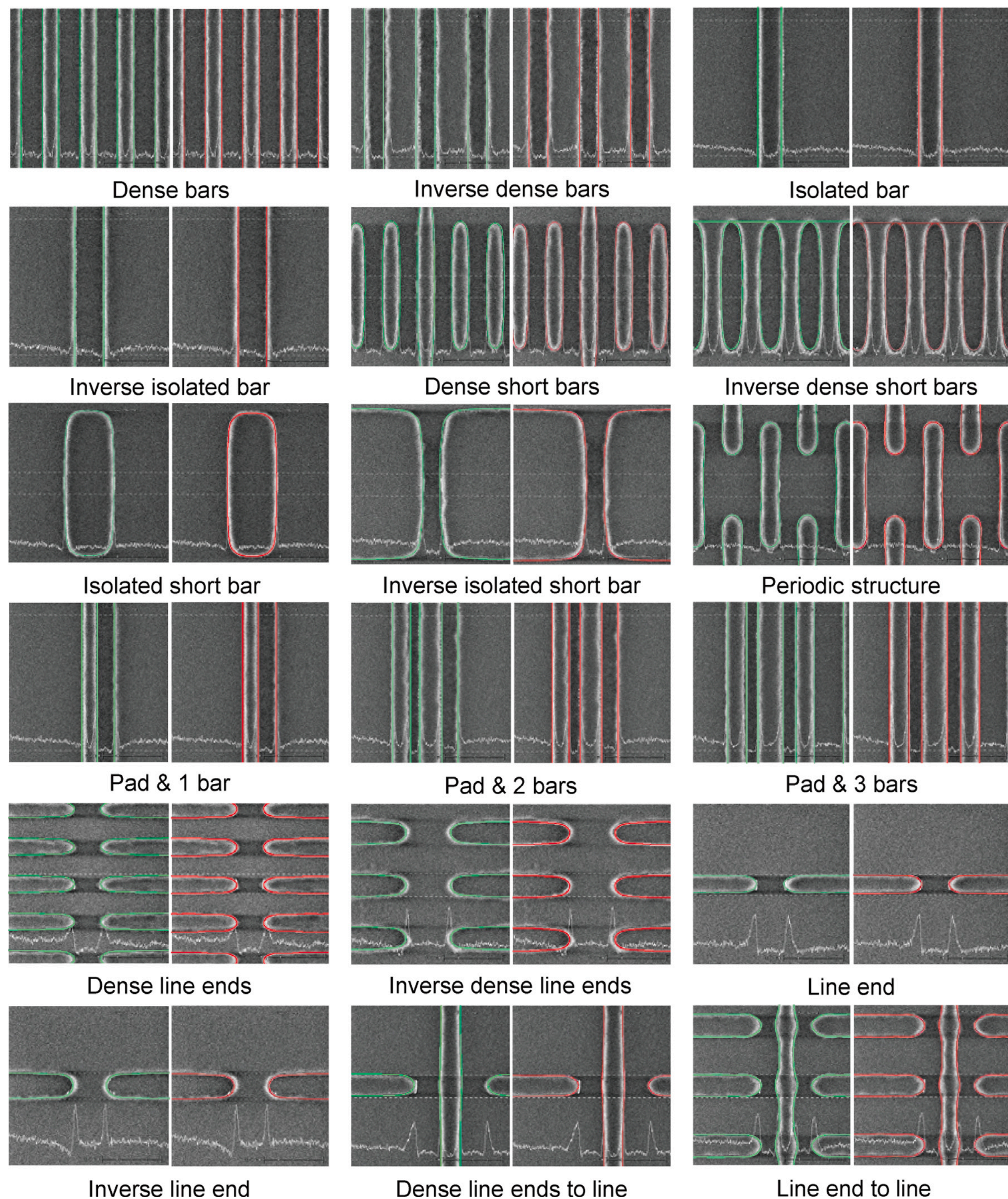

Fig. 7. Overlay of the green single-stage and red multi-stage Wiener model simulation contours on SEM images.

According to the Nyquist sampling theorem, we calculated the length of each pixel to be 40 nm. As the image size of the clip varies from 128 to 1024, the simulation area of each clip changes accordingly. The simulation experiments were conducted on hardware equipped with an Intel Core i7-10700 CPU, which features 8 cores and 16 threads, a base frequency of 2.90 GHz, and a maximum turbo boost of 4.80 GHz. Table 3 indicates that the multi-stage Wiener model consistently outperforms the single-stage Wiener model in terms of modeling time across different simulation area sizes. Before acceleration, the multi-stage model is marginally faster at smaller sizes and significantly quicker at larger sizes. After applying acceleration techniques, both models exhibit substantial improvements in speed, but the multi-stage model benefits more, maintaining a clear advantage over the single-stage model at every simulation area size.

4. Conclusion

We have reported and demonstrated a comprehensive nonlinear resist modeling solution based on a multi-stage cascaded Wiener model network. Using the proposed methods, single-stage and multi-stage Wiener models were calibrated and compared with over 3000 different test patterns. Various performance metrics and experiment results indicated that the single-stage Wiener model could already achieve production-worthy performance, while the multi-stage model would further enhance model accuracy, improve model applicability, and better computational efficiency.

In terms of model accuracy, with respect to the industrial standard that 95% of model CDs need to fall within the reference range, the multi-stage Wiener model's performance at 97.52% surpassed the

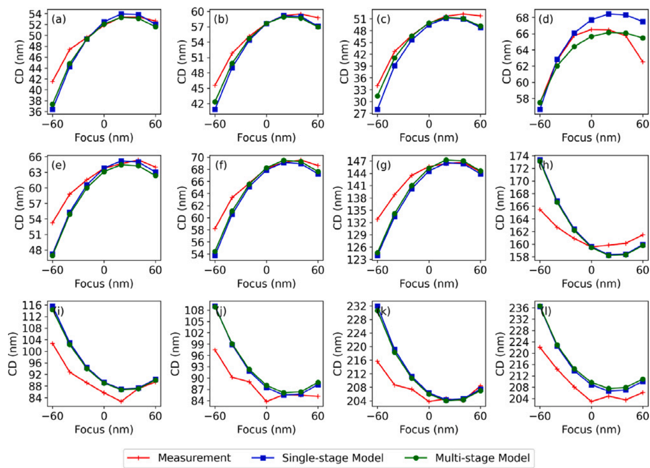

Fig. 8. Bossung plots of the single-stage and multi-stage Wiener Model under different defocus conditions for patterns (a) 64 nm lines with 260 nm pitch, (b) 64 nm lines with 1500 nm pitch, (c) 58 nm lines with 116 nm pitch, (d) 80 nm spaces with 160 nm pitch, (e) 74 nm lines with 340 nm pitch, (f) 74 nm lines with 1000 nm pitch, (g) 140 nm lines with 280 nm pitch, (h) 160 nm spaces with 320 nm pitch, (i) 80 nm line with a 60 nm space between line ends, (j) 100 nm line with a 70 nm space between line ends, (k) 60 nm line with 126 nm pitch and a 150 space nm between line ends, and (l) 70 nm line with 200 nm pitch and a 150 nm space between line ends.

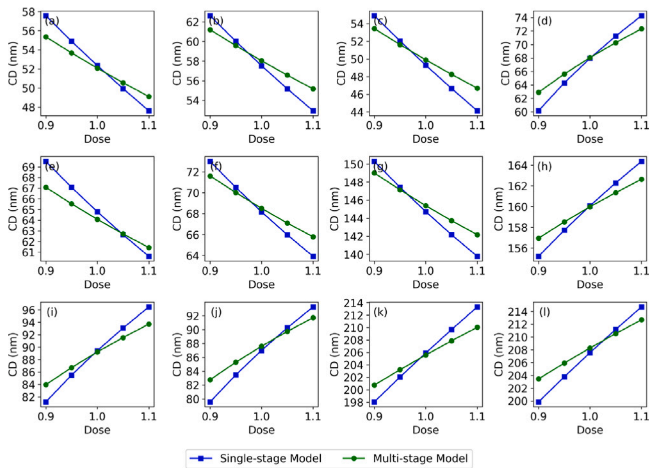

Fig. 9. Bossung plots of the single-stage and multi-stage Wiener Model under different dose conditions for patterns (a) 64 nm lines with 260 nm pitch, (b) 64 nm lines with 1500 nm pitch, (c) 58 nm lines with 116 nm pitch, (d) 80 nm spaces with 160 nm pitch, (e) 74 nm lines with 340 nm pitch, (f) 74 nm lines with 1000 nm pitch, (g) 140 nm lines with 280 nm pitch, (h) 160 nm spaces with 320 nm pitch, (i) 80 nm line with a 60 nm space between line ends, (j) 100 nm line with a 70 nm space between line ends, (k) 60 nm line with 126 nm pitch and a 150 space nm between line ends, and (l) 70 nm line with 200 nm pitch and a 150 nm space between line ends.

single-stage model's 97.13%. The multi-stage model consistently showed lower RMS and tighter error ranges across all calibration and verification categories. Additionally, the contours simulated beyond the measurement points aligned well with the structural features presented in SEM images. This not only underscored its superior accuracy and consistency but also indicated its predictions were less likely to experience extreme variances, making it a more reliable choice for practical applications.

Regarding model applicability in the process window analysis experiments, the trend of Bossung curves simulated under different defocus conditions from −60 nm to +60 nm by the single-stage Wiener model was similar to the measured curve trends, while the multi-stage Wiener model's curves were even closer. As for the performance under different dose conditions from 0.9 to 1.1, both models exhibited similar and

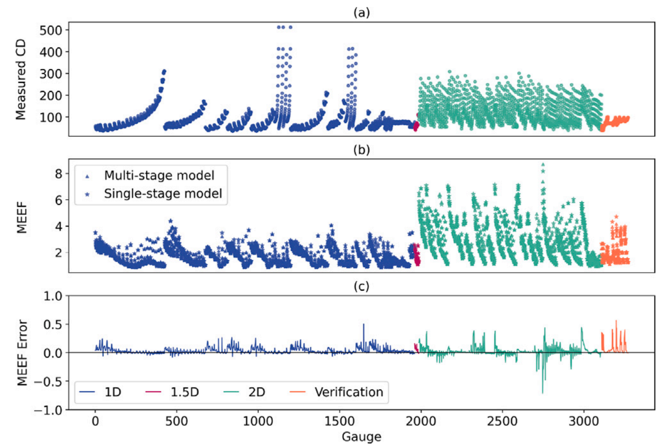

Fig. 10. (a) Measured CD, (b) MEEF and (c) MEEF error plots of the single-stage and multi-stage Wiener model.

reasonable trends in the Bossung plots. In addition, the multi-stage model generally showed better MEEF performance than the single-stage model across 68.8% of gauges, with particularly strong results in 1D (71.3%), 1.5D (84.6%), and verification data (83.5%).

In terms of computational efficiency, the proposed acceleration methods effectively reduced the resist terms for both the single-stage and multi-stage Wiener models. Due to the inherently fewer total number of terms, the multi-stage Wiener model consumed about 25% less time in forward resist modeling during mask optimization, both before and after acceleration.

CRediT authorship contribution statement

Chunxiao Mu: Writing – original draft, Validation, Software, Methodology, Investigation, Formal analysis, Data curation. **Lei Cheng:** Writing – original draft, Validation, Investigation, Formal analysis, Data curation. **Song Zhang:** Writing – review & editing, Validation, Software, Investigation, Funding acquisition, Formal analysis. **Hao Jiang:** Writing – review & editing, Supervision, Resources, Project administration, Methodology, Investigation, Funding acquisition, Conceptualization. **David H. Wei:** Writing – review & editing, Validation, Supervision, Software, Project administration, Methodology, Formal analysis, Conceptualization. **Yanlong Sun:** Writing – review & editing, Software, Methodology. **Jinlong Zhu:** Writing – review & editing, Validation. **Shiyuan Liu:** Writing – review & editing, Supervision, Resources, Project administration, Investigation, Funding acquisition.

Funding

National Natural Science Foundation of China (52205592, 52130504), Key Research and Development Plan of Hubei Province (2022BAA013), Major Program (JD) of Hubei Province (2023BAA002), and Innovation Project of Optics Valley Laboratory (OVL2023PY003).

Declaration of competing interest

The authors declare the following financial interests/personal relationships which may be considered as potential competing interests: Hao Jiang reports financial support was provided by Department of Science and Technology of Hubei Province. Shiyuan Liu reports financial support was provided by National Natural Science Foundation of China. Song Zhang reports financial support was provided by National Natural Science Foundation of China. DAVID H. WEI has patent issued to Yuwei Optica Co.,Ltd, Wuhan. If there are other authors, they declare that they have no known competing financial interests or personal relationships that could have appeared to influence the work reported in this paper.

Acknowledgments

The authors would like to express their thanks to the technical support from the Experiment Centre for Advanced Manufacturing and Technology in School of Mechanical Science and Engineering of HUST.

Data availability

Data will be made available on request.

References

[1] G. Chen, Z. Zhang, S. Li, et al., Study on deep ultraviolet computational lithography techniques, Laser Optoelectron. Prog. 59 (9) (2022) 0922007.
[2] X. Ma, S. Zhang, Y. Pan, et al., Research and progress of computational lithography, Laser Optoelectron. Prog. 59 (9) (2022) 0922008.
[3] V. Lakshmikantham, S. Leela, A.A. Martynyuk, Stability Analysis of Nonlinear Systems, Springer, 1989.
[4] S. Sastry, Nonlinear Systems: Analysis, Stability, and Control, vol. 10, Springer Science & Business Media, 2013.
[5] M. Vidyasagar, Nonlinear Systems Analysis, SIAM, 2002.
[6] A. Poonawala, Mask Design for Single and Double Exposure Optical Microlithography: An Inverse Imaging Approach, University of California, Santa Cruz, 2007.
[7] W.-C. Huang, C.-H. Lin, C.-C. Kuo, C. Huang, J. Lin, J.-H. Chen, R.-G. Liu, Y.C. Ku, B.-J. Lin, Two threshold resist models for optical proximity correction, in: Optical Microlithography XVII, Vol. 5377, SPIE, 2004, pp. 1536–1543.
[8] N.B. Cobb, A. Zakhor, M. Reihani, F. Jahansooz, V.N. Raghavan, Experimental results on optical proximity correction with variable-threshold resist model, in: Optical Microlithography X, Vol. 3051, SPIE, 1997, pp. 458–468.
[9] J. Randall, K.G. Ronse, T. Marschner, A.-M. Goethals, M. Ercken, Variable-threshold resist models for lithography simulation, in: Optical Microlithography XII, Vol. 3679, SPIE, 1999, pp. 176–182.
[10] J.J. Biafore, S. Kapasi, S.A. Robertson, M.D. Smith, The divergence of image and resist process metrics, in: Lithography Asia 2008, Vol. 7140, SPIE, 2008, pp. 586–593.
[11] J.J. Biafore, S.A. Robertson, M.D. Smith, C. Sallee, The accuracy of a calibrated PROLITH physical resist model across illumination conditions, in: Design for Manufacturability Through Design-Process Integration, Vol. 6521, SPIE, 2007, pp. 459–466.
[12] J. Vasek, J.J. Biafore, S.A. Robertson, Site portability and extrapolative accuracy of a predictive resist model, in: Design for Manufacturability Through Design-Process Integration II, Vol. 6925, SPIE, 2008, pp. 421–429.
[13] W. Gao, U. Klostermann, I. Kamohara, T. Schmoeller, K. Lucas, W. Demmerle, P. De Bisschop, J. Mailfert, Experimental validation of rigorous, 3D profile models for negative-tone develop resists, in: Optical Microlithography XXVII, Vol. 9052, SPIE, 2014, pp. 77–86.
[14] Y. Granik, N. Cobb, D. Medvedev, Application of CM0 resist model to OPC and verification, in: Optical Microlithography XIX, Vol. 6154, SPIE, 2006, pp. 1130–1136.
[15] Y. Granik, D. Medvedev, N. Cobb, Toward standard process models for OPC, in: Optical Microlithography XX, Vol. 6520, SPIE, 2007, pp. 1447–1452.
[16] N. Lafferty, K. Adam, Y. Granik, A. Torres, W. Maurer, Physically based compact models for fast lithography simulation, in: Optical Microlithography XVIII, Vol. 5754, SPIE, 2005, pp. 537–542.
[17] B. Davaji, P.A. Cook, B. Kor, Z. Luo, J. Chen, J. Clark, G. Bordonaro, V. Genova, M. Heuser, S. Ayres, et al., Deep learning for predicting CD-SEMS of NEMS devices, in: 2022 IEEE 35th International Conference on Micro Electro Mechanical Systems Conference, MEMS, IEEE, 2022, pp. 462–465.
[18] X. Ma, X. Zheng, G.R. Arce, Fast inverse lithography based on dual-channel model-driven deep learning, Opt. Express 28 (14) (2020) 20404–20421.
[19] C. Kim, S. Lee, S. Park, N.-Y. Chung, J. Kim, N. Bang, S. Lee, S. Lee, R. Boone, P. Li, et al., Machine learning techniques for OPC improvement at the sub-5 nm node, in: Extreme Ultraviolet (EUV) Lithography XI, Vol. 11323, SPIE, 2020, pp. 307–320.
[20] W. Zhong, S. Hu, Y. Ma, H. Yang, X. Ma, B. Yu, Deep learning-driven simultaneous layout decomposition and mask optimization, IEEE Trans. Comput.-Aided Des. Integr. Circuits Syst. 41 (3) (2021) 709–722.
[21] Y. Granik, Transformational invariance in compact process modeling, J. Micro/Nanolithography MEMS MOEMS 19 (1) (2020) 013502–013502.
[22] T. Ogunfunmi, Adaptive Nonlinear System Identification: The Volterra and Wiener Model Approaches, Springer Science & Business Media, 2007.
[23] G. Palm, T. Poggio, The Volterra representation and the Wiener expansion: Validity and pitfalls, SIAM J. Appl. Math. 33 (2) (1977) 195–216.
[24] H. Wei, Computer simulation of photolithographic processing, 2013, US Patent 8, 532, 964.
[25] A.Y. Kibangou, G. Favier, M.M. Hassani, Selection of generalized orthonormal bases for second-order Volterra filters, Signal Process. 85 (12) (2005) 2371–2385.
[26] K. Perev, Orthogonal approximation of Volterra series and Wiener G-functionals descriptions for nonlinear systems, Inf. Technol. Control (2019).
[27] G. Favier, A. Kibangou, R. Campello, Nonlinear systems modelling by means of generalized orthonormal basis functions, in: Invited Paper, IEEE Conference on Signals, Systems, Decision and Information Technology, SSD, Vol. 3, 2003.
[28] F. Pampaloni, J. Enderlein, Gaussian, hermite-Gaussian, and Laguerre-Gaussian beams: A primer, 2004, arXiv preprint physics/0410021.
[29] D. Wei, J. Ma, T. Wang, C. Xu, S. Zhu, M. Xiao, Y. Zhang, Laguerre-Gaussian transform for rotating image processing, Opt. Express 28 (18) (2020) 26898–26907.
[30] S.-C. Pei, C.-L. Liu, Y.-C. Lai, Discrete Laguerre Gaussian transforms and their applications, IEEE Trans. Signal Process. 64 (12) (2016) 3156–3166.
[31] P. Baluswamy, A. Weatherly, D. Kewley, P. Brooker, M. Pauzer, Practical resist model calibration, in: Optical Microlithography XVI, Vol. 5040, SPIE, 2003, pp. 1556–1569.
[32] J.D. Byers, J.S. Petersen, J.L. Sturtevant, Calibration of chemically amplified resist models, in: Advances in Resist Technology and Processing XIII, Vol. 2724, SPIE, 1996, pp. 156–162.
[33] Y. Kwon, Y. Shin, Calibration of compact resist model through CNN training, IEEE Trans. Semicond. Manuf. (2023).
[34] M. Piana, M. Bertero, Projected Landweber method and preconditioning, Inverse Probl. 13 (2) (1997) 441.